





RESEARCH ARTICLE

Range-separated density functional theory using multiresolution analysis and quantum computing

Nicolas Poirier^{1,2}  | Jakob S. Kottmann³  | Alán Aspuru-Guzik^{4,5,6,7}  |
Luc Mongeau¹  | Alireza Najafi-Yazdi^{1,2}¹Department of Mechanical Engineering, McGill University, Montreal, Quebec, Canada²Anyon Systems Inc., Dorval, Quebec, Canada³Institute for Computer Science, University of Augsburg, Augsburg, Germany⁴Chemical Physics Theory Group, Department of Chemistry, University of Toronto, Toronto, Ontario, Canada⁵Department of Computer Science, University of Toronto, Toronto, Ontario, Canada⁶Vector Institute for Artificial Intelligence, Toronto, Ontario, Canada⁷Canadian Institute for Advanced Research (CIFAR), Toronto, Ontario, Canada**Correspondence**

Nicolas Poirier and Alireza Najafi-Yazdi, Department of Mechanical Engineering, McGill University, Montreal, QC, H3A 0C3, Canada. Email: nicolas.poirier2@mail.mcgill.ca and alireza.najafiyazdi@mcgill.ca

Funding information

Mitacs, Grant/Award Number: IT26988; Google; U.S. Department of Energy, Grant/Award Number: DE-SC0019374; Natural Sciences and Engineering Research Council of Canada, Grant/Award Number: RGPIN-2016-05003; Vadasz Scholars Program; Canada Industrial Research Chairs Program; Canada 150 Research Chairs Program; Anders G. Frøseth

Abstract

Quantum computers are expected to outperform classical computers for specific problems in quantum chemistry. Such calculations remain expensive, but costs can be lowered through the partition of the molecular system. In the present study, partition was achieved with range-separated density functional theory (RS-DFT). The use of RS-DFT reduces both the basis set size and the active space size dependence of the ground state energy in comparison with the use of wave function theory (WFT) alone. The utilization of pair natural orbitals (PNOs) in place of canonical molecular orbitals (MOs) results in more compact qubit Hamiltonians. To test this strategy, a basis-set independent framework, known as multiresolution analysis (MRA), was employed to generate PNOs. Tests were conducted with the variational quantum eigensolver for a number of molecules. The results show that the proposed approach reduces the number of qubits needed to reach a target energy accuracy.

KEYWORDS

Ab initio calculations, density functional calculation, multiresolution analysis, quantum computing, variational quantum eigensolver

1 | INTRODUCTION

Since the introduction of quantum computing by Feynman,¹ a number of quantum algorithms have been developed to reduce the computational cost of specific problems.^{2–5} One of these problems is the calculation of the ground state energy of molecular systems.⁶ So far, only a few instances of this problem are suited for noisy intermediate-scale quantum (NISQ) computers.⁷ This limitation is due to the intrinsic

noise and errors of NISQ devices. In order for additional problem instances to benefit from a quantum advantage, there must be a sharing of the computational load between NISQ computers and classical computers. Embedding techniques have been developed to partition the molecules involved in the electronic structure problem.^{8–12} One such approach is range-separated density functional theory (RS-DFT),^{8,13} where a portion of the molecular system is treated with a variational quantum algorithm (VQA)^{14,15} while the remainder is treated with

This is an open access article under the terms of the [Creative Commons Attribution](https://creativecommons.org/licenses/by/4.0/) License, which permits use, distribution and reproduction in any medium, provided the original work is properly cited.

© 2024 The Authors. *Journal of Computational Chemistry* published by Wiley Periodicals LLC.

Kohn-Sham density functional theory (DFT).¹⁶ In the present study, strategies that improve the accuracy of RS-DFT when combined with the variational quantum eigensolver (VQE)^{17,18} are explored. Pair natural orbitals (PNOs)^{19–21} and multiresolution analysis (MRA) were used to improve the compactness of the qubit Hamiltonian.²²

The Kohn-Sham DFT method is a core component of RS-DFT. In Kohn-Sham DFT, the solution accuracy depends on an effective one-electron potential. This potential in turn depends on a functional of the electron density. But the needed functional is not exact.²³ One challenge is that the potential term which accounts for electron exchange often does not decay as required with position.²⁴ This issue is addressed in range-separated DFT through the partition of the two-electron Coulomb repulsion operator into the sum of long-range and short-range terms based on the interelectronic distance. At long range, static correlation is predominant. Dynamic correlation is more important at short range. The dynamic correlation corresponds to the correlated motion of the electrons due to the Coulomb repulsion, whereas the static correlation is the correlated motion of the electrons caused by the presence of nearly-degenerate configurations.²⁵ The static correlation is important, for example, when a molecule is dissociated into fragments.²⁶ As DFT can be inaccurate for static correlation, it is used to handle the short-range term. The long-range term is handled with a wave function theory (WFT) method, here the VQE. The separation between short-range and long-range terms depends on a range-separation parameter. From the perspective of WFT and quantum computing, the use of range separation diminishes the impact of two factors on the accuracy of ground state energy estimates. These factors are the basis set size and the active space size. The decreased impact is due to a lowering of the limit at a singularity in the long-range electron repulsion potential. This lower limit leads to the disappearance of the electron cusp in the wave function.²⁷

The performance of both embedded DFT and VQE depends on the strategy for the generation of molecular orbitals (MOs). Typically, the MOs used in VQE calculations are canonical orbitals that diagonalize the Fock matrix. However, these orbitals are suboptimal for the recovery of the correlation between electron pairs, unless all the generated MOs are included in the active space. A better recovery of the correlation is achieved with a truncated set of pair natural orbitals (PNOs).^{19–21} Both canonical orbitals and PNOs can be generated through a linear combination of atomic orbitals (LCAO). This approach leads to a compact representation of the MOs, but it is costly for large systems if a high precision is needed. The LCAO method is also prone to basis set superposition errors.²² One alternative method, known as multiresolution analysis (MRA), provides systematic accuracy improvements through the efficient representation of MOs on a real-space grid.²² The generation of PNOs with MRA was adopted for the present study because MRA-PNOs represent the most accurate orbitals for the chosen level of theory, in this case Møller-Plesset (MP2) perturbation theory.^{28,29} Additionally, the basis set independence of the MRA approach facilitates the study of the behavior of RS-DFT.

One major advantage of employing MRA and PNOs on a quantum computer is that fewer qubits are needed to reach a target accuracy for a given number of electrons. This was demonstrated in Kottmann et al.,³⁰ where it was shown that MRA-PNOs could be used to simulate

the umbrella reaction of ammonia with only 12 to 18 qubits. The equivalent simulation with canonical LCAO orbitals would require 50 to 100 qubits to reach the same accuracy. A similar approach involving Daubechies wavelets has also been implemented by Hong et al.³¹

To the knowledge of the authors, the embedded DFT and MRA-PNO methods have not yet been utilized simultaneously. The present study combines these two approaches with the overall goal of extending the range of molecular systems which could benefit from a quantum advantage for the calculation of the ground state energy. More specifically, the objective is to increase the accuracy of ground state energy estimates for a limited amount of quantum resources. The overall objective includes three specific aims. One aim is to show that pair natural orbitals can provide a greater accuracy than canonical orbitals for the same number of qubits (i.e., active space size). Another aim is to identify if there are instances where range separation with pair natural orbitals can outperform WFT as well as Kohn-Sham DFT. The final aim is to show that it is beneficial to employ range separation to treat the long-range interactions with the VQE and the short-range ones with DFT. This approach, if successful, could broaden the range of practical chemistry problems that could benefit from the availability of larger NISQ computers. The results illustrate the combined effects of multiple methods—namely, range-separated DFT, pair natural orbitals, and the VQE—on benchmark systems.

The next section of this paper describes the theoretical framework for the use of MRA-PNOs with range-separated DFT in the context of quantum computing. The theory section includes a brief overview of range-separated DFT and MRA-PNOs. This section also includes a description of the range-separated active space Hamiltonian and an introduction to the VQE. In the methodology section, the implementation details of the range-separated calculations are presented. In the following section, results that involve molecules which range in size from H₂ to H₂O are provided and interpreted. Final remarks are included in the last section of the paper.

2 | THEORY

2.1 | Range-separated density functional theory

Range-separated DFT can be used to approximate the ground state energy of molecular systems. The Hamiltonian which describes these systems is

$$\hat{H} = \hat{T} + \hat{V}_{ne} + \hat{V}_{ee}, \quad (1)$$

where \hat{T} is the kinetic energy operator, \hat{V}_{ne} is the nuclear-electron Coulomb attraction energy operator, and \hat{V}_{ee} is the electron-electron Coulomb repulsion operator. The ground state energy, E_0 , of the Hamiltonian can be obtained with the help of a two-step minimization formula²³

$$E_0 = \min_{\rho} \left[\min_{\Psi \rightarrow \rho} \langle \Psi | \hat{T} + \hat{V}_{ee} | \Psi \rangle + \int v_{ne}(\mathbf{r}) \rho(\mathbf{r}) d\mathbf{r} \right], \quad (2)$$

where ρ is the electron density, Ψ is an N-electron antisymmetric wave function, $v_{ne}(\mathbf{r})$ is the nuclear-electron potential, and \mathbf{r} denotes the three-dimensional spatial coordinates of an electron. The inner minimization procedure corresponds to Levy's constrained-search formula for a density functional,³²

$$F[\rho] = \min_{\Psi \rightarrow \rho} \{ \langle \Psi | \hat{T} + \hat{V}_{ee} | \Psi \rangle \}. \quad (3)$$

This functional could be employed using uniquely the DFT approach, but the idea behind range separation is to separate the electron repulsion potential into the sum of a long-range term and a short-range term. The former term is assigned to a wave function theory (WFT) solver since this term mostly involves static correlation. The latter term is allocated to a DFT solver because this term mostly involves dynamic correlation. The electronic repulsion operator is separated as follows:

$$\hat{V}_{ee} = \hat{V}_{ee}^{lr,\mu} + \hat{V}_{ee}^{sr,\mu}, \quad (4)$$

where lr and sr indicate long-range and short-range, respectively, and $\mu \geq 0$ is a range-separation parameter.¹³ When μ is zero, the long-range term vanishes, while the short-range term becomes zero when μ approaches infinity.

Insertion of the range-separated terms into the constrained search formula yields the following equation for the ground-state energy:¹³

$$E_0 = \min_{\Psi} \left[\langle \Psi | \hat{T} + \hat{V}_{ee}^{lr,\mu} | \Psi \rangle + E_H^{sr,\mu}[\rho(\Psi)] + E_{xc}^{sr,\mu}[\rho(\Psi)] + \int v_{ne}(\mathbf{r})\rho(\Psi) d\mathbf{r} \right], \quad (5)$$

where $E_H^{sr,\mu}[\rho]$ and $E_{xc}^{sr,\mu}[\rho]$ are the short-range Hartree and exchange-correlation energy functionals, respectively. The former functional corresponds to

$$E_H^{sr,\mu}[\rho] = \frac{1}{2} \int \rho(\mathbf{r})\rho(\mathbf{r}') v_{ee}^{sr,\mu}(\mathbf{r},\mathbf{r}') d\mathbf{r}d\mathbf{r}', \quad (6)$$

where the short-range electronic repulsion potential is defined as

$$v_{ee}^{sr,\mu}(\mathbf{r},\mathbf{r}') = \frac{f(\mu,\mathbf{r},\mathbf{r}')}{|\mathbf{r}-\mathbf{r}'|}. \quad (7)$$

The image of the range-separation function $f(\mu,\mathbf{r},\mathbf{r}')$ is over a span from 0 to 1. The upper limit of 1 is obtained when μ is 0 and the lower limit of 0 is reached as μ approaches infinity. One example of a range-separation function is the Yukawa potential.^{33,34} The long-range electronic repulsion potential is defined as¹³

$$v_{ee}^{lr,\mu}(\mathbf{r},\mathbf{r}') = v_{ee}(\mathbf{r},\mathbf{r}') - v_{ee}^{sr,\mu}(\mathbf{r},\mathbf{r}') = \frac{1-f(\mu,\mathbf{r},\mathbf{r}')}{|\mathbf{r}-\mathbf{r}'|}, \quad (8)$$

where v_{ee} is the electronic repulsion potential.

Equation (5) for the ground-state energy would be exact and independent of μ if the exact short-range exchange-correlation functional was available. However, in practice, the ground state energy varies

with μ . When μ is 0, $\hat{V}_{ee}^{lr,\mu}$ vanishes and the Kohn-Sham DFT equations are recovered.¹⁶ On the other hand, the short-range terms vanish and the WFT equations are recovered when μ approaches infinity.

2.2 | Orbital generation with multiresolution analysis

Unlike with the LCAO methodology, MRA-PNOs are generated using a basis-set-independent black-box procedure. The resulting PNOs correspond to the best possible PNOs for the size of the truncated orbital space. The use of MRA to generate the PNOs eliminates basis set effects in the analysis. The utilization of MRA-PNOs in lieu of canonical orbitals also leads to a reduction of the number of qubits needed to reach a target accuracy.³⁰

Before the generation of the PNOs, occupied MOs are constructed using a self-consistent field method (e.g., Kohn-Sham DFT). The occupied MOs ϕ_i are obtained iteratively using the Lippmann-Schwinger integral equation^{22,35}

$$\phi_i(\mathbf{r}) = -2 \int G_{\alpha}(\mathbf{r},\mathbf{r}') \hat{V}(\mathbf{r}') \phi_i(\mathbf{r}') d\mathbf{r}', \quad (9)$$

where $G_{\alpha}(\mathbf{r},\mathbf{r}')$ is the three-dimensional bound-state Helmholtz (BSH) Green's function and $\hat{V}(\mathbf{r})$ is the potential energy operator. The Green's function is defined as

$$G_{\alpha}(\mathbf{r},\mathbf{r}') = \frac{\exp(-\alpha|\mathbf{r}-\mathbf{r}'|)}{4\pi|\mathbf{r}-\mathbf{r}'|}, \quad (10)$$

where $\alpha = \sqrt{-2\varepsilon_i}$ and ε_i is the eigenvalue that is associated with ϕ_i . A more detailed overview of MRA is provided by Harrison et al.,²² who were the first to develop a strategy for solving the Kohn-Sham DFT equations with MRA. A review of MRA in the context of quantum chemistry was also written by Bischoff.³⁶

After the generation of the occupied MOs, PNOs are constructed using second-order Møller-Plesset (MP2) perturbation theory.²⁸ Each PNO is associated with a pair of occupied MOs. The importance of each PNO in the MP2 solution is quantified by an occupation number. These occupation numbers are later used to select the active space. It is important to note that the number of PNOs generated, which is known as the rank, is not fixed.²⁹ Along with the occupied MOs, the PNOs constitute the basis functions to approximate the multi-determinant wave function of Equation (5). The PNOs for different occupied MO pairs are not orthogonal, however. They are therefore orthonormalized using a Cholesky decomposition.^{30,37}

2.3 | Range-separated active space Hamiltonian

To create a second-quantized Hamiltonian, only systems with singlet spin symmetry were considered. For such systems, the Hamiltonian is expressed as²⁵

$$\hat{H} = \Omega_0 + \sum_{pq} \Omega_{pq} \hat{E}_{pq} + \frac{1}{2} \sum_{pqrs} \Omega_{pqrs} \hat{e}_{pqrs}, \quad (11)$$

where Ω_0 , Ω_{pq} , and Ω_{pqrs} are constants. As for the operators \hat{E}_{pq} and \hat{e}_{pqrs} , they correspond to

$$\hat{E}_{pq} = \sum_{\sigma \in \{\uparrow, \downarrow\}} \hat{a}_{p\sigma}^\dagger \hat{a}_{q\sigma} \quad (12)$$

and

$$\hat{e}_{pqrs} = \hat{E}_{pq} \hat{E}_{rs} - \hat{E}_{ps} \hat{E}_{qr}, \quad (13)$$

respectively, where $\hat{a}_{p\sigma}^\dagger$ is a fermionic creation operator and $\hat{a}_{q\sigma}$ is a fermionic annihilation operator. The index, σ , indicates whether a molecular spin-orbital involves a spin-up (\uparrow) or a spin-down (\downarrow) electron. The indices p and q are used to identify MOs.

The calculation of the ground state energy of the system Hamiltonian is prohibitively expensive for systems containing more than one dozen electrons. Additional constraints must therefore be imposed for larger systems in order to reduce the computational cost. In the present study, the set of all MOs was divided into active and inactive spaces. The active space contains both occupied and virtual MOs. The active orbitals were utilized to generate additional configurations in the multi-determinant wave function. The remaining occupied MOs form the inactive space and are present in every configuration. Active MOs are labelled u, v, x, y . Inactive MOs are labelled i, j, k, l . General MOs are labelled p, q, r, s .²⁵ Labels A and I refer to the active and inactive spaces, respectively.

The system Hamiltonian is modified through both the inclusion of an active space and the separation of the electron repulsion operator. The Hamiltonian is the superposition of three separate terms:

$$\hat{H} = \hat{H}_I^I + \hat{H}_A^I + \hat{H}^{sr}, \quad (14)$$

where \hat{H}_I^I is the inactive long-range Hamiltonian, \hat{H}_A^I is the active long-range Hamiltonian, and \hat{H}^{sr} is the short-range Hamiltonian. The derivation of each of these terms is found in the works of Hedegård et al.³⁸ and Rossmannek et al.⁸

For systems with singlet spin symmetry, the Hamiltonian may be simplified. For example, the inactive long-range Hamiltonian is

$$\hat{H}_I^I = \sum_i \left(h_{ii} + f_{ii}^{I,I} \right) + V_{nn}, \quad (15)$$

where h_{pq} are one-electron integrals that take into account the kinetic energy and the nuclear-electron Coulomb attraction energy. The integrals are defined as

$$h_{pq} = \langle \phi_p(\mathbf{r}) | \left(-\frac{1}{2} \nabla^2 + v_{ne}(\mathbf{r}) \right) | \phi_q(\mathbf{r}) \rangle. \quad (16)$$

The entries $f_{ii}^{I,I}$ of the long-range inactive Fock matrix correspond to

$$f_{pq}^{I,I} = h_{pq} + \sum_i \left(2g_{pqii}^{I,I} - g_{piqi}^{I,I} \right), \quad (17)$$

where $g_{pqrs}^{I,I}$ is a long-range two-electron integral

$$g_{pqrs}^{I,I} = \langle \phi_p(\mathbf{r}) \phi_r(\mathbf{r}') | v_{ee}^{I,I}(\mathbf{r}, \mathbf{r}') | \phi_q(\mathbf{r}) \phi_s(\mathbf{r}') \rangle. \quad (18)$$

The long-range electron repulsion potential $v_{ee}^{I,I}(\mathbf{r}, \mathbf{r}')$ must be replaced by $v_{ee}^{sr}(\mathbf{r}, \mathbf{r}')$ or $v_{ee}(\mathbf{r}, \mathbf{r}')$ in order to obtain the short-range two-electron integral, g_{pqrs}^{sr} , or the standard two-electron integral, g_{pqrs} , respectively. It should be noted that the inactive long-range Hamiltonian is applied to a fixed portion of the wave function during the calculation. This is not the case for the active long-range Hamiltonian, which corresponds to

$$\hat{H}_A^I = \sum_{uv} f_{uv}^{I,I} \hat{E}_{uv} + \frac{1}{2} \sum_{uvxy} g_{uvxy}^{I,I} \hat{e}_{uvxy}. \quad (19)$$

The implementation of the short-range Hamiltonian \hat{H}^{sr} presents some challenges. One of them is that the short-range Hartree-exchange-correlation energy, E_{Hxc}^{sr} , is nonlinear with respect to the one-electron reduced density matrix (1-RDM), where a 1-RDM entry is defined as³⁹

$$D_{pq} = \langle \Psi | \hat{E}_{pq} | \Psi \rangle. \quad (20)$$

The nonlinearity can be expressed as the following inequality:

$$E_{Hxc}^{sr}[\rho_{ref} + \Delta\rho] \neq E_{Hxc}^{sr}[\rho_{ref}] + E_{Hxc}^{sr}[\Delta\rho], \quad (21)$$

where the change in electron density is $\Delta\rho(\mathbf{r})$, and the reference density is $\rho_{ref}(\mathbf{r})$. The electron density is obtained from the 1-RDM as

$$\rho = \sum_{pq} \phi_p(\mathbf{r}) \phi_q(\mathbf{r}) D_{pq}. \quad (22)$$

The inequality of Equation (21) poses a challenge since the Hamiltonian must be linear. As a solution, Pedersen³⁹ developed a technique for linearizing the DFT portion of the Hamiltonian. The consequence of this linearization is that the Hamiltonian must be updated iteratively during the calculation.

The short-range Hamiltonian is then divided into a state-averaged term \hat{H}_{SA}^{sr} and an active term \hat{H}_A^{sr} . The state-averaged term depends on the 1-RDM of the previously completed iteration (i), but its expectation value remains constant during the ongoing iteration ($i+1$). The expectation value of the active term varies during each iteration. The state-averaged term is

$$\hat{H}_{SA}^{sr} = \sum_i J_{ii}^{I, sr} - \sum_{uv} \left[\left(\frac{1}{2} J_{uv}^{A, (i), sr} + v_{xc, uv}^{sr}[\rho^{(i)}] \right) D_{uv}^{A, (i)} \right] + E_{xc}^{sr}[\rho^{(i)}], \quad (23)$$

where

$$J_{pq}^{(i), sr} = \sum_{rs} g_{pqrs}^{sr} D_{rs}^{(i)} \quad (24)$$

and

$$v_{xc,pq}^{sr}[\rho^{(i)}] = \langle \phi_p | v_{xc}^{sr}[\rho^{(i)}] | \phi_q \rangle. \quad (25)$$

The variables $D_{rs}^{(i)}$ and $\rho^{(i)}$ correspond to the 1-RDM and the electron density of the latest completed iteration, respectively. The active short-range Hamiltonian is

$$\hat{H}_A^{sr} = \sum_{uv} \left[\left(J_{uv}^{l, sr} + J_{uv}^{A, (i), sr} + v_{xc, uv}^{sr}[\rho^{(i)}] \right) \hat{E}_{uv} \right]. \quad (26)$$

All operators in the long-range and short-range Hamiltonians are only applied to active MOs. These Hamiltonians are summed and the results are rearranged to match the form of Equation (11). The result is the following equation:

$$\hat{H} = \Omega_0 + \sum_{uv} \Omega_{uv} \hat{E}_{uv} + \frac{1}{2} \sum_{uvxy} \Omega_{uvxy} \hat{e}_{uvxy}, \quad (27)$$

where

$$\Omega_0 = \sum_i \left(h_{ii} + f_{ii}^{l, sr} + j_{ii}^{l, sr} \right) - \sum_{uv} \left[\left(\frac{1}{2} J_{uv}^{A, (i), sr} + v_{xc, uv}^{sr}[\rho^{(i)}] \right) D_{uv}^{A, (i)} \right] + E_{xc}^{sr}[\rho^{(i)}] + V_{nn}, \quad (28)$$

$$\Omega_{uv} = f_{uv}^{l, sr} + j_{uv}^{l, sr} + J_{uv}^{A, (i), sr} + v_{xc, uv}^{sr}[\rho^{(i)}], \quad (29)$$

and

$$\Omega_{uvxy} = g_{uvxy}^{l, sr}. \quad (30)$$

During each iteration, the ground state energy and the 1-RDM for the Hamiltonian are computed with a WFT method such as the VQE.¹⁷ The Hamiltonian is updated using the latest computed 1-RDM at the start of each iteration. The process is repeated until the termination criterion, such as the maximum energy difference, is met.^{8,38} It is also important to note that the final wave function must be an N -electron wave function, where N is the number of electrons in the system. This constraint can be enforced in the WFT algorithm.

2.4 | Variational quantum eigensolver

Almost a decade ago, Peruzzo, McClean, et al. introduced the VQE algorithm.¹⁷ This algorithm approximates the ground state energy of a Hamiltonian. It leverages the combined computational power of quantum and classical computers. It is therefore a hybrid algorithm. In the VQE, the quantum computer measures the expectation value of a qubit Hamiltonian

$$\langle \hat{H} \rangle = \langle \Psi(\theta) | \hat{H} | \Psi(\theta) \rangle, \quad (31)$$

where $|\Psi(\theta)\rangle$ is a parameterized quantum state and θ is a set of parameters. The quantum state is generated through the application

of a parameterized unitary ansatz, $U(\theta)$, to an initial state, $|\Psi_{init}\rangle$, which results in

$$|\Psi(\theta)\rangle = U(\theta)|\Psi_{init}\rangle. \quad (32)$$

The classical computer, on the other hand, is utilized to minimize the expectation value of the Hamiltonian. This is achieved through the variation of the quantum state parameters with an optimization algorithm. During each iteration, the classical computer receives the expectation value from the quantum computer before generating a new ansatz with updated parameters. This process is repeated until convergence is obtained. The optimal expectation value represents an approximation of the ground state energy¹⁷

$$E_0 \approx \min_{\theta} \langle \Psi(\theta) | \hat{H} | \Psi(\theta) \rangle. \quad (33)$$

In the present work, two ansätze were evaluated. First, the separable pair ansatz (SPA) was used.⁴⁰ The SPA is a classically tractable ansatz which was employed as a benchmark. The SPA ansatz produces a separable pair wave function

$$|\Psi_{SP}\rangle = \prod_{k=1}^{N/2} |\Psi_k\rangle, \quad (34)$$

where N is the number of electrons and $|\Psi_k\rangle$ is an electron pair function. A pair function corresponds to

$$|\Psi_k\rangle = \sum_m c_m^k |\phi_{m_1}^k\rangle \otimes |\phi_{m_1}^k\rangle, \quad (35)$$

where c_m^k is a real coefficient and $|\phi_{m_1}^k\rangle$ is the qubit representing a spin-up molecular spin-orbital (MSO).³⁰

The second ansatz is the k -UpCCGSD ansatz. The acronym UpCCGSD stands for unitary coupled-cluster with generalized single and paired double excitations.⁴¹ Unlike the separable pair ansatz, it is classically intractable except for small systems that require less than 100 qubits. The use of paired double excitations (i.e., with spin-orbitals from the same spatial orbital) leads to shallower circuits than for unpaired double excitations. The use of generalized excitations in lieu of non-generalized excitations results in improved accuracy. The generalized excitations do not restrict the annihilation operators to occupied orbitals and the creation operators to virtual orbitals.⁴¹

Although the MOs are commonly held constant in the VQE, it is possible to allow them to vary.⁴²⁻⁴⁴ An orbital optimization approach can be beneficial when static correlation is important. Orbitals can be optimized through the application of the unitary operator $e^{\hat{\kappa}}$. The result is the state

$$|\Psi(\theta, \kappa)\rangle = e^{\hat{\kappa}} |\Psi(\theta)\rangle, \quad (36)$$

where κ are the orbital rotation parameters and the corresponding operator is

$$\hat{\kappa} = \sum_{pq} \kappa_{pq} (\hat{E}_{pq} - \hat{E}_{qp}). \quad (37)$$

The orbital rotation parameters are determined by solving the following Newton-Raphson equation on a classical computer

$$\mathbf{H}\kappa = -\mathbf{g}, \quad (38)$$

where \mathbf{H} and \mathbf{g} are the electronic Hessian and gradients, respectively. Both \mathbf{H} and \mathbf{g} depend on the two-electron reduced density matrix (2-RDM) of $|\Psi(\theta)\rangle$. The 2-RDM is obtained by executing the VQE on a quantum computer. The VQE must be executed each time accurate estimates of \mathbf{H} and \mathbf{g} are necessary. These new estimates are needed because the Newton-Raphson equation, Equation (38), is solved iteratively.⁴³ The estimation of the 2-RDM of state $|\Psi(\theta)\rangle$ is a bottleneck in the orbital optimization procedure. It has a worst-case cost that scales as $O(M^4)$, where M is the number of spatial MOs. Techniques have been developed to obtain the 2-RDM at a lower cost. Some of these techniques involve the enforcement of N -representability conditions,⁴⁵ the partitioning of operators,^{46–51} the use of classical shadows,⁵² or the utilization of more efficient fermion-to-qubit mappings.⁵³ The need for the 2-RDM in other quantum algorithms should help accelerate research in the reduction of 2-RDM estimation costs. For instance, the 2-RDM can be employed to mitigate errors⁴⁵ or to evaluate properties such as energy gradients and multipole moments.^{51,54}

3 | METHODOLOGY

The computational techniques outlined in the theory section required the tools from multiple software packages. One of these was MADNESS,⁵⁵ which is utilized to generate occupied MOs as well as PNOs using MRA. The MADNESS code has been modified in several ways for this project. These modifications include the addition of functions that enable the application of a long-range exchange operator. Functions that facilitate the use of range-separated functionals were also added. The Yukawa potential^{33,34} was adopted to perform the range separation

$$v_{ee}^{sr,\mu}(\mathbf{r}, \mathbf{r}') = \frac{f_{\text{Yuk}}(\mu, \mathbf{r}, \mathbf{r}')}{|\mathbf{r} - \mathbf{r}'|} = \frac{\exp(-\mu|\mathbf{r} - \mathbf{r}'|)}{|\mathbf{r} - \mathbf{r}'|}. \quad (39)$$

This is because MADNESS relies on the BSH Green's function, shown in Equation (10), to obtain MOs. The similarity between the BSH Green's function and the Yukawa potential made the latter convenient to implement in MADNESS. One important drawback of using the Yukawa potential is that short exchange-correlation potentials are sometimes only available for erf-based range separation

$$v_{ee}^{sr,\mu_{\text{erf}}}(\mathbf{r}, \mathbf{r}') = \frac{f_{\text{erf}}(\mu_{\text{erf}}, \mathbf{r}, \mathbf{r}')}{|\mathbf{r} - \mathbf{r}'|} = \frac{1 - \text{erf}(\mu_{\text{erf}}|\mathbf{r} - \mathbf{r}'|)}{|\mathbf{r} - \mathbf{r}'|}, \quad (40)$$

where erf is the error function and μ_{erf} is a specific range separation parameter. In Libxc,⁵⁶ the functional library that was used for this

project, only short-range correlation functionals which are separated using the error function are provided. The range-separation parameter must, therefore, be converted when employing these functionals. The proposed conversion factor is

$$\mu_{\text{erf}} \approx 0.5\mu. \quad (41)$$

The derivation of the conversion factor is provided in the supplementary material. The conversion was needed for the short-range LYP correlation functional.⁵⁷ The available short-range B88 exchange functional⁵⁸ relied on the Yukawa potential. Both functionals were utilized to conduct the range-separated calculations.

The Tequila package⁵⁹ was used to generate the ansatz⁶⁰ and the quantum circuit. It was also employed to apply the Jordan-Wigner transformation,^{61,62} execute the VQE, and compute the 1-RDM. In the VQE, the Broyden-Fletcher-Goldfarb-Shanno (BFGS)^{63–66} optimizer was employed along with the Qulacs⁶⁷ quantum computer simulator. The other functions that were needed for this project were implemented in a private repository. They will soon be added to the official Tequila main code branch. These include functions to compute range-separated integrals, to generate the active space Hamiltonian of Equation (11), and to iteratively improve the 1-RDM. Canonical LCAO orbitals were also generated with PySCF^{68,69} in order to compare the performance of MRA-PNOs and canonical LCAO MOs. Some of the calculations used the full configuration interaction (FCI) solver or the orbital optimization solver. Both solvers are available in PySCF. Reference energies were computed with Psi4 unless otherwise specified.⁷⁰

The active MOs were selected based on two factors. The first was the occupation numbers of the PNOs. The second was the relationship between each PNO and an occupied MO pair. The PNO with the highest occupation number was first selected. The related MO pair was also added to the active space. The PNO with the next highest occupation number along with the associated MO pair was then selected. This process was repeated until the desired number of active MOs was reached.

4 | RESULTS AND DISCUSSION

4.1 | Influence of range-separation parameter

In order to understand the impacts of the active space size and the range-separation parameter on the performance of the range-separated VQE, the energy of a few molecules at their equilibrium geometries was computed. These molecules are LiH, BH, BeH₂, and H₂O. Their equilibrium geometries are provided in the supplementary material. Plots of the relation between the range-separated energy and the range-separation parameter are shown in Figure 1. The range-separated energy was obtained by utilizing MRA-PNOs in complete active space configuration interaction (CASCI) calculations. The resulting energy was compared to the DFT energy and a reference *ab initio* value. The notations CAS(N, M) and CASCI(N, M) indicate that N electrons and M spatial MOs are in the active space.

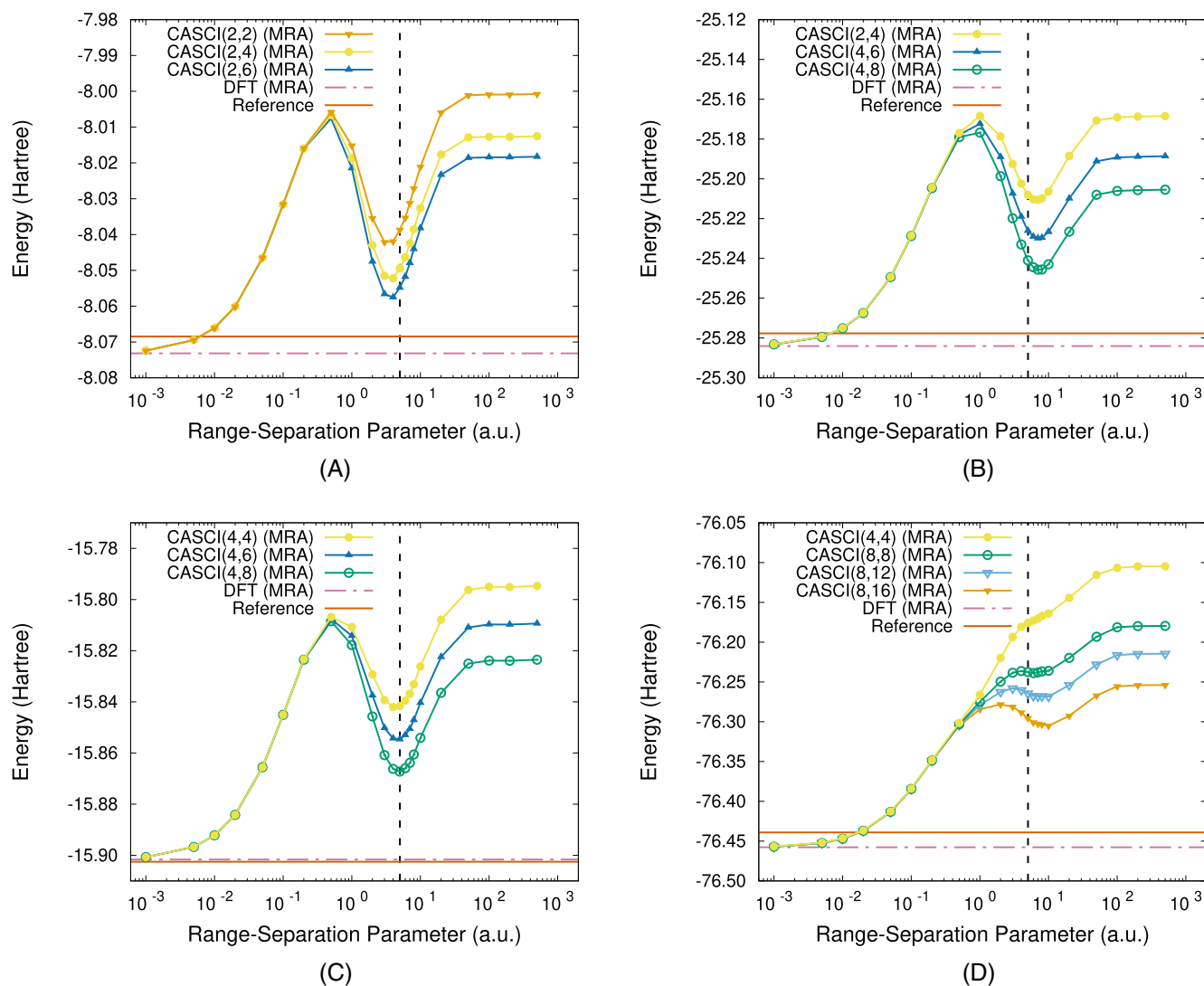


FIGURE 1 The energy of (A) LiH, (B) BH, (C) BeH₂, and (D) H₂O as a function of the range-separation parameter for multiple active spaces. The range-separated results are compared to the Kohn-Shan DFT energy at the basis set limit and to a reference energy that approximates the exact energy at the basis set limit. For all calculations involving DFT, the short-range B88 exchange⁵⁸ and the short-range LYP correlation⁵⁷ functionals were utilized. For (A) LiH, the reference is the FCI energy in the cc-pCVQZ basis.⁷¹ For (B) BH, it is the CISDTQ energy in the cc-pCTVZ basis.⁷¹ For (C) BeH₂, it is the icMRCI+Q energy in the aug-cc-pV5Z basis, where icMRCI+Q stands for the internally contracted multireference configuration interaction method with Langhoff and Davidson corrections.⁷² For (D) H₂O, it is the extrapolated coupled cluster (CCSD(T)) energy, where the cc-pCV5Z and cc-pCV6Z bases were used for the extrapolation.²⁵ The vertical dashed line indicates the range-separation parameter of 5.0 a.u. that was selected for the other PES calculations.

As expected, the range-separated energy as $\mu \rightarrow 0$ tends towards the DFT energy, as shown in Figure 1. On the other hand, the range-separated curves converged to the WFT solution for the chosen active space as $\mu \rightarrow \infty$. At equilibrium, the optimal point along the range-separated curve occurred at μ between 1 a.u. and 10 a.u. if the energy as $\mu \rightarrow 0$ was not considered. This is due to the reduced impact of the basis set size as μ is decreased. The reduction in basis set size dependence is caused by a singularity in the long-range electron repulsion potential, which occurs at $|\mathbf{r}-\mathbf{r}'| \rightarrow 0$. The decrease of μ leads to a lower limit at the singularity and, therefore, the disappearance of the electron cusp in the wave function.²⁷ The elimination of the cusp is an incentive for the use of potentials at a smaller μ . It leads

to wave functions that can be accurately described with a smaller basis set and a smaller active space. The impact of μ on the active space size dependence can be seen in Figure 1C. For $\mu < 1$ a.u., the choice of active space has virtually no effect on the energy.

One challenge with range-separated approaches is that the choice of a range-separation parameter is not trivial. The optimal parameter depends on a multitude of factors. A lowering of μ results in a decrease in the basis set size and the active space size dependence of the ground state energy. This in turn leads to a reduction in computational cost. Conversely, the accuracy of the short-range exchange-correlation functional decreases as μ is lowered except, possibly, as μ approaches 0. This is because of the way the functionals are constructed.

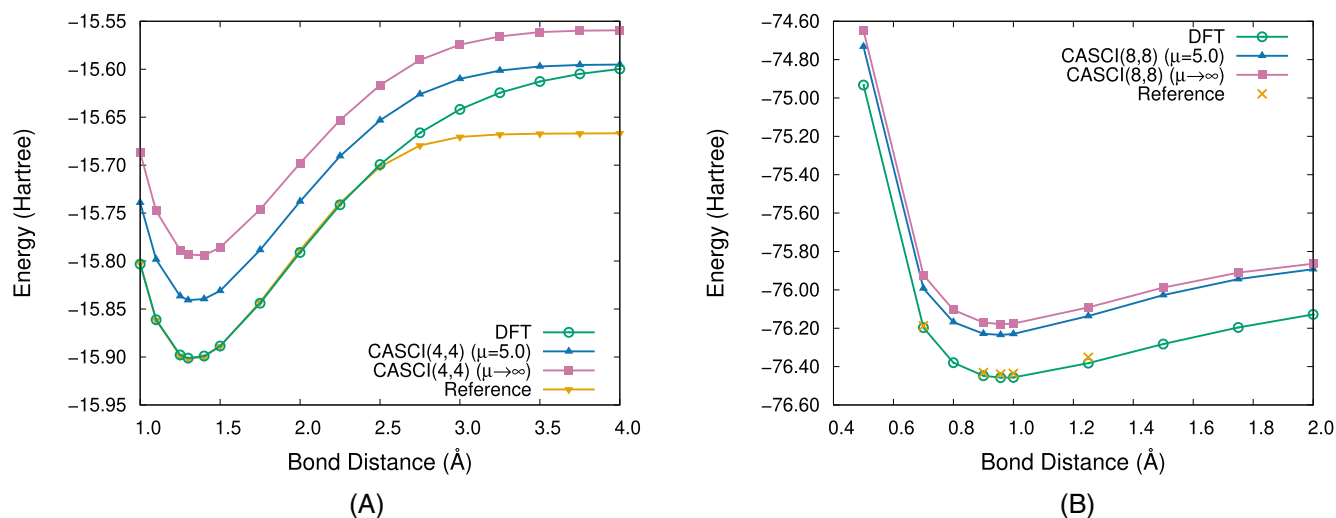


FIGURE 2 The energy of (A) BeH₂ and (B) H₂O as their bonds are symmetrically stretched. The range-separated results are compared to the Kohn-Shan DFT energy at the basis set limit and to a reference energy that approximates the exact energy at the basis set limit. For all calculations involving DFT, the short-range B88 exchange⁵⁸ and the short-range LYP correlation⁵⁷ functionals were utilized. For (A) BeH₂, the reference is the icMRCI+Q energy in the aug-cc-pV5Z basis.⁷² For (B) H₂O, it is the sum of the relative icMRCI+Q energy⁷⁴ and the extrapolated coupled cluster (CCSD(T)) energy at equilibrium.²⁵ For the relative energy, the aug-cc-pV5Z and aug-cc-pV6Z bases were used for the extrapolation, whereas the cc-pCV5Z and cc-pCV6Z bases were used for the absolute energy.

One strategy for constructing the functional involves taking the asymptotic expansion of the exchange-correlation energy as $\mu \rightarrow \infty$. The range-separated functional is then generated by interpolating between the expansion as $\mu \rightarrow \infty$ and a density functional approximation (e.g., B88) at $\mu \rightarrow 0$.⁷³ Therefore, if μ is too small, the errors introduced by the approximate range-separated functional outweigh the cost benefits caused by the disappearance of the electron cusp. Upon added computational resources, if available, μ can be increased to reduce the errors caused by the functional. In the present work, a range-separation parameter of 5.0 a.u. was selected since it appeared to provide a suitable balance between basis set dependence and functional accuracy.

4.2 | Impact of molecular geometry

The potential energy surfaces (PESs) of H₂, LiH, BH, BeH₂, and H₂O were investigated in order to determine the accuracy of the range-separated approach for multiple geometries. The curves were obtained through the symmetric variation of the bond distances, while the equilibrium bond angles remained constant. The PESs of BeH₂ and H₂O are shown in Figure 2.

The maximum absolute error (MAX) and the non-parallelity error (NPE) with respect to the reference energy were computed to quantify the potential benefits of range separation. The NPE corresponds to the difference between the maximum and minimum errors along the PES.⁴¹ The MAX and NPE for the PESs of the analyzed molecules are shown in Figure 3. Tables listing the MAX and NPE for these PESs are also provided in the supplementary material.

In general, the use of range separation leads to a reduction in absolute errors compared to the use of WFT alone. The range-separated

solver is not always able to outperform DFT. Near the equilibrium geometry, DFT outperforms range-separation and WFT due to its smaller basis set size dependence. The accuracy of DFT decreases for H₂ and BeH₂ at larger bond distances. This is due to the inability of the exchange-correlation functional to properly describe static correlation. For H₂ and BeH₂, range separation results in a more consistent improvement in accuracy compared to the use of only DFT with the BLYP functional. For the other examined molecules, the BLYP functional remains more accurate even at large bond distances for the chosen active space sizes.

4.3 | Accuracy of the ansatz

Another factor which has an influence on the energy accuracy is the choice of ansatz in the VQE solver. The PESs for H₂, LiH, BH, and BeH₂ were obtained using the SPA ansatz to determine the impact of this factor. Dissociation curves computed with the SPA and UpCCGSD ansatz for BeH₂ are shown in Figure 4.

The MAX and NPE errors were computed in order to quantify the magnitude of the improvements brought by range separation with one specific ansatz. The MAX and NPE for the PESs of the examined molecules are shown in Figure 5. Tables listing the MAX and NPE for these PESs are also provided in the supplementary material.

Overall, these results show that, even when employing the VQE, the use of range separation provides an increase in accuracy. This increase in accuracy is due to the ability of short-range DFT to handle dynamical correlation. For most molecules and ansätze, the VQE also provides results which are similar in accuracy to those obtained with a CASCI solver. As expected, this is the case for H₂ when employing the

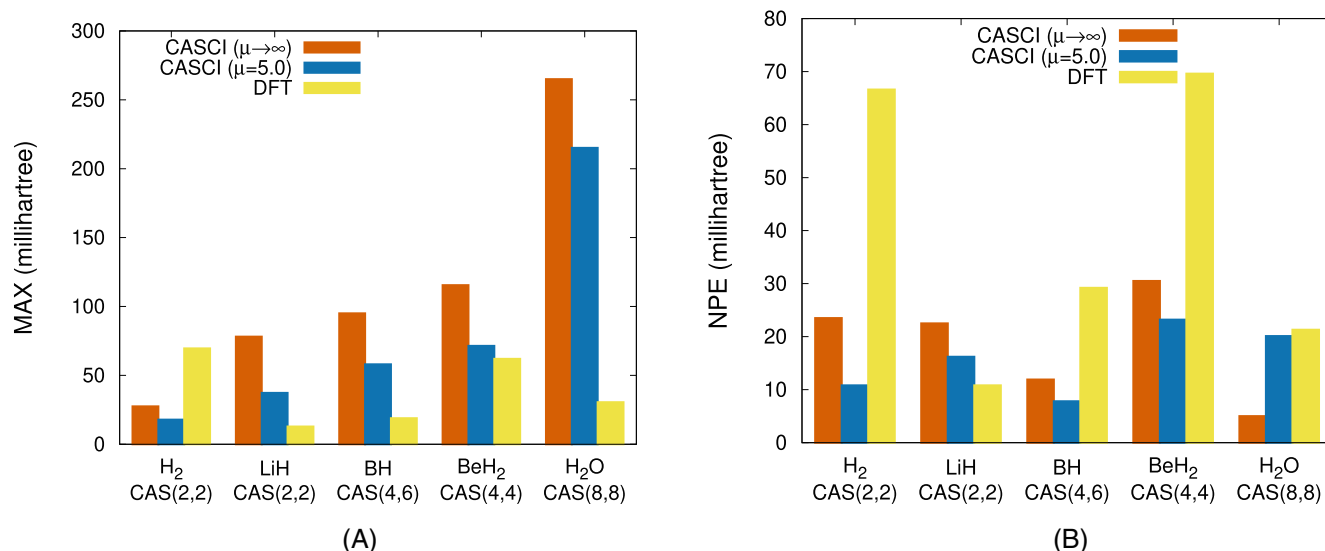


FIGURE 3 The maximum absolute error (MAX) and the non-parallelity error (NPE), with respect to the reference energy, for the PESs of multiple molecules. The range-separated results were obtained with a CASCI solver. For all calculations involving DFT, the short-range B88 exchange⁵⁸ and the short-range LYP correlation⁵⁷ functionals were utilized. For H₂, the reference is the non-relativistic *ab initio* limit.⁷⁵ For LiH, it is the FCI energy in the cc-pCVQZ basis.⁷¹ For BH, the reference is the CISDTQ energy in the cc-pCTVZ basis.⁷¹ For BeH₂, it is the icMRCI+Q energy in the aug-cc-pV5Z basis.⁷² For H₂O, it is the sum of the relative icMRCI+Q energy⁷⁴ and the extrapolated coupled cluster (CCSD(T)) energy at equilibrium.²⁵ For the relative energy, the aug-cc-pV5Z and aug-cc-pV6Z bases were used for the extrapolation, whereas the cc-pCV5Z and cc-pCV6Z bases were used for the absolute energy.

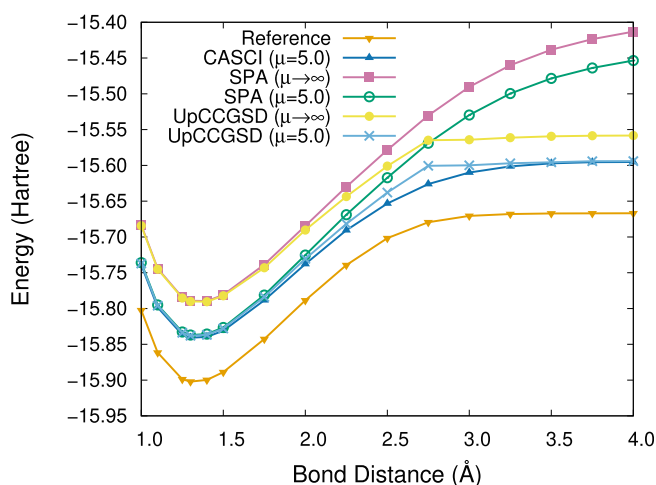


FIGURE 4 The energy of BeH₂ as it is symmetrically stretched. The energy was computed with the VQE and either the SPA or the UpCCGSD ansatz. The VQE calculations were conducted at $\mu = 5.0$ a. u. and $\mu \rightarrow \infty$. The SPA energy is compared to the CASCI energy at $\mu = 5.0$ a.u. and to a reference energy that approximates the exact energy at the basis set limit. This reference is the icMRCI+Q energy in the aug-cc-pV5Z basis.⁷² For all calculations involving DFT, the short-range B88 exchange⁵⁸ and the short-range LYP correlation⁵⁷ functionals were utilized. With the exception of the icMRCI+Q energy, an active space containing 4 MOs and 4 electrons was used.

SPA ansatz.⁷⁶ The SPA can also recover most of the correlation for LiH since there is only one occupied active MO from which PNO pairs are generated. The other occupied MO remains frozen. The SPA also

performs well for BH. However, the shortcomings of the SPA ansatz become apparent for BeH₂ as it struggles to recover the static correlation for large bond distances in that case. This is to be expected since the SPA ansatz only creates entanglement between PNOs that are associated with the same occupied MO. A well-constructed classically intractable ansatz, which generates more entanglement, should outperform the SPA ansatz. This is the case for the UpCCGSD ansatz, although it fails to recover some of the correlation for bond distances near 2.75 Å.

4.4 | Impact of orbitals

The method chosen for the generation of basis orbitals was found to impact the accuracy of range-separated calculations. Although the main focus of this work was MRA-PNOs, results obtained with PNOs were compared to other results determined with canonical orbitals. This clarified the distinction between the improvements brought by range separation and those brought by PNOs. These PNOs were obtained with MRA, following the approach of Reference 29, in order to avoid effects caused by the utilization of predetermined basis sets. The canonical orbitals were computed with predetermined LCAO basis sets. This approach was chosen because the generation of virtual canonical orbitals with an adaptive basis is not trivial. The lowest of these orbitals tend to be diffuse and have an energy which is close to zero. This is a consequence of the MRA orbital optimization procedure, which favors orbitals with low energies. Similar orbitals also appear if diffuse functions are included in

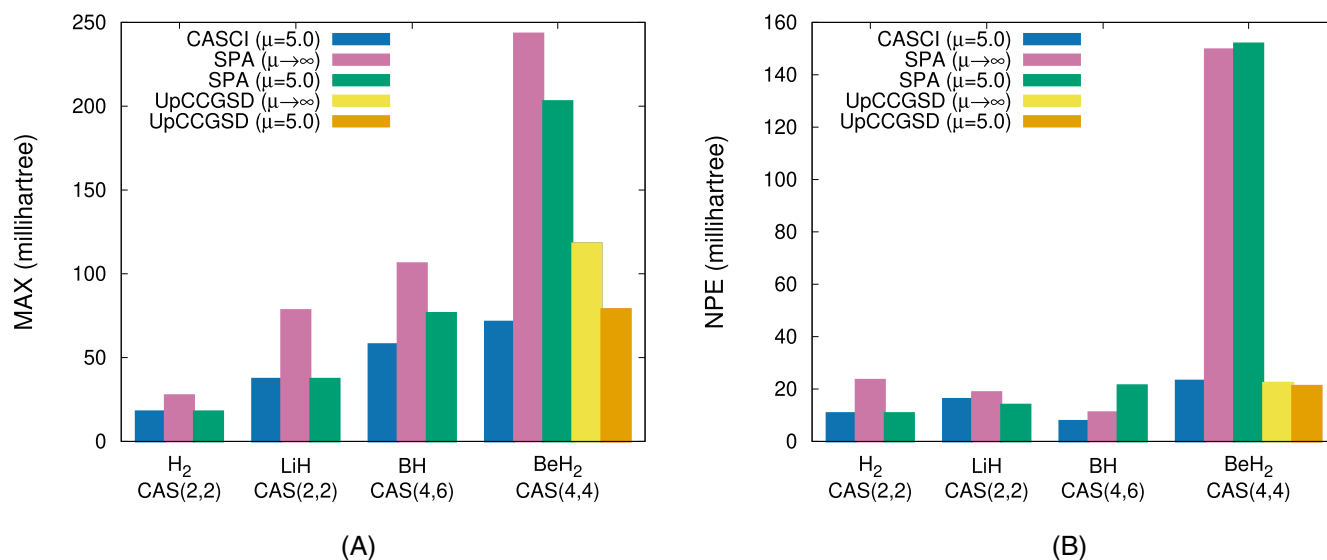


FIGURE 5 The maximum absolute error (MAX) and the non-parallelity error (NPE), with respect to the reference energy, for the PESs of multiple molecules. The range-separated results were obtained with a CASCI solver as well as the SPA and UpCCGSD ansatz. For H₂, the reference is the nonrelative *ab initio* limit.⁷⁵ For LiH, it is the FCI energy in the cc-pCVQZ basis.⁷¹ For BH, the reference is the CISDTQ energy in the cc-pCTVZ basis.⁷¹ For BeH₂, it is the icMRCI+Q energy in the aug-cc-pV5Z basis.⁷²

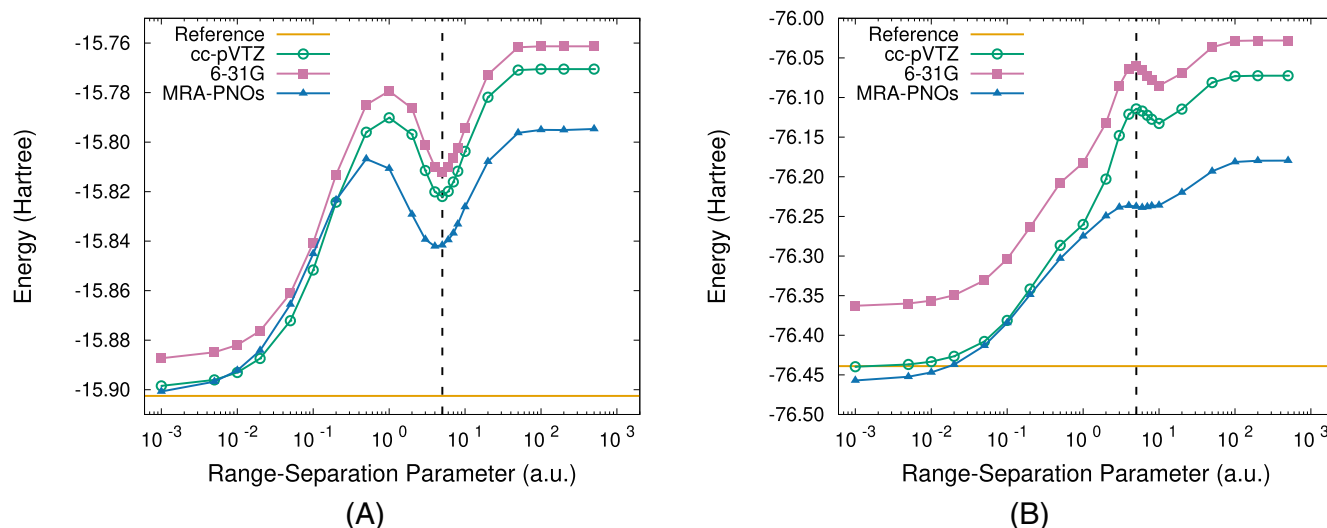


FIGURE 6 The energy of (A) BeH₂ and (B) H₂O at their equilibrium geometries as a function of the range-separation parameter. The range-separated energy was calculated with a CASCI solver and either MRA-PNOs or canonical LCAO MOs. The range-separated energy is compared to a reference energy that approximates the exact energy at the basis set limit. For (A) BeH₂, the reference energy was the icMRCI+Q energy in the aug-cc-pV5Z basis.⁷² For (B) H₂O, it was the extrapolated coupled cluster (CCSD(T)) energy, where the cc-pCV5Z and cc-pCV6Z bases were used for the extrapolation.²⁵ For all calculations involving DFT, the short-range B88 exchange⁵⁸ and the short-range LYP correlation⁵⁷ functionals were utilized. With the exception of the reference energies, the active space for (A) BeH₂ contained 4 MOs and 4 electrons while the active space for H₂O had 8 MOs and 8 electrons. The vertical dashed line indicates the range-separation parameter of 5.0 a.u. that was selected for the other PES calculations.

LCAO basis sets (e.g., aug-cc-pVXZ⁷⁷). Non-augmented basis sets were selected to avoid this issue and to provide a fair comparison between PNOs and canonical MOs. This comparison is shown in Figure 6, where the energy of BeH₂ and H₂O at equilibrium is shown as a function of the range-separation parameter. Two LCAO basis

sets, 6-31G⁷⁸ and cc-pVTZ,⁷⁹ were selected for the comparison. For both molecules, the 6-31G basis set led to the formation of 13 MOs while the cc-pVTZ basis set led to the generation of 58 MOs. The MO with the lowest orbital energy was frozen for both MRA-PNOs and canonical MOs. The remaining MOs with the lowest orbital

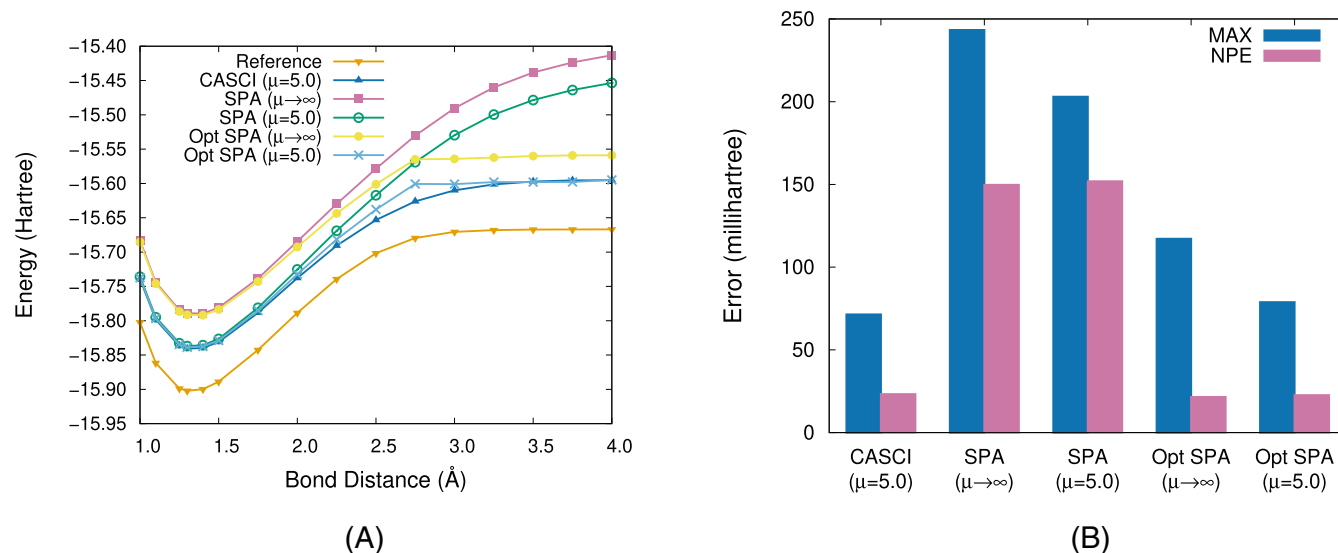


FIGURE 7 (A) The energy of BeH₂ as a function of bond distance as the molecule is symmetrically stretched. The energy was computed with the VQE and the SPA ansatz with either unoptimized (MRA-PNO) or optimized (Opt SPA) orbitals. The VQE calculations were conducted at $\mu = 5.0$ a.u. and $\mu \rightarrow \infty$. The SPA energy is compared to the CASCI energy at $\mu = 5.0$ a.u. and to a reference energy that approximates the exact energy at the basis set limit. This reference is the icMRCI+Q energy in the aug-cc-pV5Z basis.⁷² For all calculations involving DFT, the short-range B88 exchange⁵⁸ and the short-range LYP correlation⁵⁷ functionals were utilized. (B) The maximum absolute error (MAX) and the non-parallelity error (NPE) of the PESs with respect to the reference energy. With the exception of the reference energy, an active space containing 4 MOs and 4 electrons was used.

energies were selected for the active space of the canonical MOs. A comparison between the errors associated with the canonical and PNO approaches, at $\mu = 5.0$ a.u., is also provided in the supplementary material.

As shown in Figure 6, the energy obtained with canonical orbitals in the cc-pVTZ basis nearly coincides with the MRA-PNO energy for smaller range-separation parameters (i.e., near DFT-only). This is because the energy in this range of μ does not depend on the virtual orbitals in the active space. Conversely, the energy does depend on the overall basis set size. The quality of the occupied Kohn-Sham orbitals increases from 6-31G to cc-pVTZ, where the latter yields results similar to the MRA representation, which can be assumed to represent the basis set limit.²² The quality of the MOs in the active space has a greater importance as μ tends to infinity (i.e., near WFT-only). This results in greater errors for the canonical orbitals in both LCAO basis sets.

These comparisons indicate that, given a certain number of qubits (i.e., a certain active space size), MRA-PNOs can provide more accurate results than canonical LCAO MOs. This is partly because PNOs are generated such that they enable a compact representation of the molecular system. As a result, a greater portion of the dynamical correlation is included in the active space. It must be noted that the generation of orthonormal PNOs constitutes a bottleneck in the MRA-PNO approach. Alternatively, PNOs could be generated using the LCAO method. But the utilization of MRA enables the construction of PNOs at the basis set limit. This eliminates the need to worry about possible artifacts from the use of predetermined basis sets. Observed effects can instead be explained by the choice of surrogate

model, in this case MP2, and the number of requested orbitals. Pragmatically, it is safe to assume that PNOs obtained with MRA have a similar accuracy to PNOs obtained with basis sets between aug-cc-pVTZ and aug-cc-pVQZ.²⁹

It can also be beneficial to re-optimize the orbitals between VQE iterations following the procedure described by Equations (36)–(38). This is shown in Figure 7A, which contains dissociation curves for BeH₂. To quantify the accuracy of orbital optimization, the MAX and NPE errors for BeH₂ are also shown in Figure 7B. Tables listing the MAX and NPE for these PESs are shown in the supplementary material.

As shown in Figure 7, orbital optimization leads to smaller errors as the bond distance is increased. This is due to the multi-configurational nature of the wave function for BeH₂ near dissociation. But orbital optimization cannot fully compensate for the error caused by the SPA ansatz at a bond distance of 2.75 Å. The use of an ansatz with greater entanglement generation is needed to reduce the error at that bond distance. The utilization of range separation also leads to a reduction in absolute errors over the entire PES when compared to the non-separated energy curves.

5 | CONCLUSIONS

The objective of this study was to increase the accuracy of molecular ground state energy estimates given a limited amount of quantum resources. The proposed approach could broaden the range of practical chemistry problems amenable to larger NISQ computers.

Two possible pathways were explored in order to establish a protocol. The first pathway is the treatment of different portions of the molecular system with different theoretical frameworks. The second pathway is the judicious choice of MOs for the description of the wave function. The chosen strategy combined the separation of short- and long-range interactions with range-separated DFT, the use of PNOs in the active space, and the approximation of the ground state wave function with the VQE.

The treatment of short-range interactions with a DFT solver and of large-range interactions with a WFT solver provided multiple benefits for the molecules considered. For instance, the utilization of DFT led to smaller basis set size and active space size requirements. This is because DFT recovers most of the dynamical correlation with a one-electron potential. But certain DFT functionals, such as BLYP, were inaccurate when molecules like H_2 and BeH_2 were near dissociation. The utilization of WFT to treat long-range interactions in these cases resulted in a better recovery of the static correlation. Overall, the range-separated DFT approach was more accurate than only WFT given the same number of qubits. It was also found to be more accurate than the Kohn-Sham DFT approach in some cases.

It was observed that the utilization of PNOs, in lieu of canonical MOs, improved the accuracy of range-separated DFT calculations. This is partly because the generated PNOs provided a compact representation of the molecular system. This results in the inclusion of a larger portion of the dynamical correlation in the active space. One additional advantage of the MRA-PNO approach is that MRA is a basis-set free approach. Errors due to the selection of a specific LCAO basis set are therefore excluded from the energy calculations. Furthermore, the generation of occupation numbers during the construction of the PNOs results in a more systematic selection of the active space. The PNOs may not necessarily form the best MOs, however. For instance, it may be beneficial to iteratively optimize the MOs during the VQE calculation when an ansatz, such as SPA, is utilized. This is the case for BeH_2 when the bond distances exceed 2.5 Å. But an ansatz that generates more entanglement, such as the UpCCGSD ansatz, provides a relatively accurate representation of the wave function without the need for further optimization of the PNOs. Yet, even the UpCCGSD ansatz is unable to recover some of the correlation that CASCI recovers for BeH_2 at bond distances of 2.75 Å. A more accurate ansatz is needed to recover this correlation.⁷⁶

Although the proposed protocols were successful in the reduction of quantum resource requirements, additional work is needed to improve their reliability. One important source of error is the approximate nature of the range-separated DFT functionals. The development of more accurate functionals could lead to a reduction of the optimal range-separation parameter. This would result in a decrease of both the active space size dependence and the amount of quantum resources needed. One possible solution to improve the functional accuracy is to include the on-top pair density as suggested by Hapka et al.⁸⁰ Another area of interest is the selection of the optimal range-separation parameter. This selection depends on multiple factors, such as the choice of functional and the amount of quantum resource available. Lastly, alternative methods for the generation of orbitals may be

better suited than those used in the present study.^{81,82} In some instances, it may be beneficial to generate more accurate orbitals. In other cases, it might be preferable to accelerate their generation even at the cost of reduced accuracy.

ACKNOWLEDGMENTS

The authors would like to thank members of the Matter lab at the University of Toronto for their advice and insightful discussions. This project was supported by NSERC Discovery grant RGPIN-2016-05003, Mitacs grant IT26988, the Vadasz Scholars Program, and the U.S. Department of Energy under Award No. DE-SC0019374. Alán Aspuru-Guzik acknowledges generous support from Google, Inc. in the form of a Google Focused Award. Alán Aspuru-Guzik also acknowledges support from the Canada Industrial Research Chairs Program and the Canada 150 Research Chairs Program. Some computations were conducted on the Béluga supercomputer, which was made possible due to the support of Calcul Québec (calculquebec.ca) and the Digital Research Alliance of Canada (alliancecan.ca). Furthermore, we thank Anders G. Frøseth for his generous support.

CONFLICT OF INTEREST STATEMENT

The authors declare no potential conflict of interests.

DATA AVAILABILITY STATEMENT

The data that support the findings of this study are available from the corresponding author upon reasonable request.

ORCID

Nicolas Poirier  <https://orcid.org/0009-0002-4589-0804>

Jakob S. Kottmann  <https://orcid.org/0000-0002-4156-2048>

Alán Aspuru-Guzik  <https://orcid.org/0000-0002-8277-4434>

Luc Mongeau  <https://orcid.org/0000-0003-0344-227X>

REFERENCES

- [1] R. P. Feynman, *Int. J. Theor. Phys.* **1982**, 21, 467.
- [2] P. W. Shor, Proceedings 35th Annual Symposium on Foundations of Computer Science, pp. 124-34. **1994**.
- [3] L. K. Grover, Proceedings of the twenty-eighth annual ACM symposium on Theory of computing-STOC'96, ACM Press, pp. 212-219. **1996** <http://portal.acm.org/citation.cfm?doid=237814.237866>
- [4] S. Lloyd, *Science* **1996**, 273, 1073.
- [5] E. Farhi, J. Goldstone, S. Gutmann, A Quantum Approximate Optimization Algorithm. **2014**.
- [6] D. S. Abrams, S. Lloyd, *Phys. Rev. Lett.* **1999**, 83, 5162.
- [7] J. Preskill, *Quantum* **2018**, 2, 79.
- [8] M. Rossmannek, P. Kl, P. J. Ollitrault, I. Tavernelli, *J Chem Phys* **2021**, 154, 114105.
- [9] M. Rossmannek, F. Pavošević, A. Rubio, I. Tavernelli, Quantum Embedding Method for the Simulation of Strongly Correlated Systems on Quantum Computers. **2023**.
- [10] H. Ma, M. Govoni, G. Galli, *Npj Comput. Mater.* **2020**, 6, 85.
- [11] B. Huang, M. Govoni, G. Galli, *PRX Quantum* **2022**, 3, 010339.
- [12] C. Nicholas, A Hybrid Classical/Quantum Approach for Large-Scale Studies of Quantum Systems with Density Matrix Embedding Theory. **2016**.
- [13] A. Savin, *Beyond the Kohn-Sham Determinant*, Vol. 1, World Scientific, Singapore **1995**, p. 129.

- [14] M. Cerezo, A. Arrasmith, R. Babbush, S. C. Benjamin, S. Endo, K. Fujii, J. R. McClean, K. Mitarai, X. Yuan, L. Cincio, P. J. Coles, N. Reviews, *Physics* **2021**, 3, 625.
- [15] K. Bharti, A. Cervera-Lierta, T. H. Kyaw, T. Haug, S. Alperin-Lea, A. Anand, M. Degroote, H. Heimonen, J. S. Kottmann, T. Menke, W.-K. Mok, S. Sim, L.-C. Kwok, A. Aspuru-Guzik, *Rev. Mod. Phys.* **2022**, 94, 015004.
- [16] W. Kohn, L. J. Sham, *Phys. Rev.* **1965**, 140, A1133.
- [17] A. Peruzzo, J. McClean, P. Shadbolt, M.-H. Yung, X.-Q. Zhou, P. J. Love, A. Aspuru-Guzik, J. L. O'Brien, *Nat. Commun.* **2014**, 5, 4213.
- [18] J. R. McClean, J. Romero, R. Babbush, A. Aspuru-Guzik, *New J. Phys.* **2016**, 18, 023023.
- [19] C. Edmiston, M. Krauss, *J Chem Phys* **1965**, 42, 1119.
- [20] R. Ahlrichs, W. Kutzelnigg, *Theor. Chim. Acta* **1968**, 10, 377.
- [21] C. Riplinger, F. Neese, *J Chem Phys* **2013**, 138, 034106.
- [22] R. J. Harrison, G. I. Fann, T. Yanai, Z. Gan, G. Beylkin, *J Chem Phys* **2004**, 121, 11587.
- [23] R. G. Parr, W. Yang, *Density-Functional Theory of Atoms and Molecules*, Oxford University Press, Oxford, UK **1989**.
- [24] T. Yanai, D. P. Tew, N. C. Handy, *Chem. Phys. Lett.* **2004**, 393, 51.
- [25] T. Helgaker, P. Jorgensen, J. Olsen, *Molecular Electronic-Structure Theory*, John Wiley & Sons, Ltd, Chichester, UK **2000**.
- [26] R. J. Bartlett, J. F. Stanton, *Applications of Post-Hartree-Fock Methods: A Tutorial*, John Wiley & Sons, Ltd, Hoboken, NJ, USA **1994**, p. 65.
- [27] A. Savin, *On degeneracy, near-degeneracy and density functional theory*, Vol. 4, Elsevier, Amsterdam, Netherlands **1996**, p. 327.
- [28] C. Møller, M. S. Plesset, *Phys. Rev.* **1934**, 46, 618.
- [29] J. S. Kottmann, F. A. Bischoff, E. F. Valeev, *J Chem Phys* **2020**, 152, 074105.
- [30] S. Jakob, P. S. Kottmann, T. Tamayo-Mendoza, A. Aspuru-Guzik, *J Phys Chem Lett* **2021**, 12, 663.
- [31] C.-L. Hong, T. Tsai, J.-P. Chou, P.-J. Chen, P.-K. Tsai, Y.-C. Chen, E.-J. Kuo, D. Srolovitz, H. Alice, Y.-C. Cheng, H.-S. Goan, *PRX Quantum* **2022**, 3, 020360.
- [32] M. Levy, *Proc Natl Acad Sci* **1979**, 76, 6062.
- [33] H. Yukawa, *Nippon Sugaku-Buturigakkwai Kizi Dai 3 Ki* **1935**, 17, 48.
- [34] A. Savin, H.-J. Flad, *Int. J. Quantum Chem.* **1995**, 56, 327.
- [35] M. H. Kalos, *Phys. Rev.* **1962**, 128, 1791.
- [36] F. A. Bischoff, in *State of The Art of Molecular Electronic Structure Computations: Correlation Methods, Basis Sets and More*, volume 79 of *Advances in Quantum Chemistry* (Eds: L. U. Ancarani, P. E. Hoggan), Academic Press, Cambridge, MA, USA **2019**, p. 3.
- [37] Benoît, *Bulletin Géodésique* **1924**, 2, 67.
- [38] E. D. Hedegård, S. Knecht, J. S. Kielberg, H. J. A. Jensen, M. Reiher, *J Chem Phys* **2015**, 142, 224108.
- [39] J. K. Pedersen, Ph.D. thesis. University of Southern Denmark **2004**.
- [40] J. S. Kottmann, A. Aspuru-Guzik, *Phys. Rev. A* **2022**, 105, 032449.
- [41] J. Lee, W. J. Huggins, M. Head-Gordon, K. B. Whaley, *J. Chem. Theory Comput.* **2019**, 15, 311.
- [42] T. Takeshita, N. C. Rubin, Z. Jiang, E. Lee, R. Babbush, J. R. McClean, *Phys. Rev. X* **2020**, 10, 011004.
- [43] W. Mizukami, K. Mitarai, Y. O. Nakagawa, T. Yamamoto, T. Yan, Y. y. Ohnishi, *Phys Rev Res* **2020**, 2, 033421.
- [44] I. O. Sokolov, P. Kl, P. J. Ollitrault, D. Greenberg, J. Rice, M. Pistoia, I. Tavernelli, *J Chem Phys* **2020**, 152, 124107.
- [45] N. C. Rubin, R. Babbush, J. McClean, *New J. Phys.* **2018**, 20, 053020.
- [46] A. F. Izmaylov, T.-C. Yen, I. G. Ryabinkin, *Chem. Sci.* **2019**, 10, 3746.
- [47] A. F. Izmaylov, T.-C. Yen, R. A. Lang, V. Verteletskyi, *J. Chem. Theory Comput.* **2020**, 16, 190.
- [48] V. Verteletskyi, T.-C. Yen, A. F. Izmaylov, *J Chem Phys* **2020**, 152, 124114.
- [49] T.-C. Yen, V. Verteletskyi, A. F. Izmaylov, *J. Chem. Theory Comput.* **2020**, 16, 2400.
- [50] A. Zhao, A. Tranter, W. M. Kirby, S. F. Ung, A. Miyake, P. J. Love, *Phys. Rev. A* **2020**, 101, 062322.
- [51] X. Bonet-Monroig, R. Babbush, T. E. O'Brien, *Phys. Rev. X* **2020**, 10, 031064.
- [52] A. Zhao, N. C. Rubin, A. Miyake, *Phys. Rev. Lett.* **2021**, 127, 110504.
- [53] Z. Jiang, A. Kalev, W. Mruzckiewicz, H. Neven, *Quantum* **2020**, 4, 276.
- [54] G. Gidofalvi, D. A. Mazziotti, *J Chem Phys* **2007**, 126, 024105.
- [55] R. J. Harrison, G. Beylkin, F. A. Bischoff, J. A. Calvin, G. I. Fann, J. Fosso-Tande, D. Galindo, J. R. Hammond, R. Hartman-Baker, J. C. Hill, J. Jia, J. S. Kottmann, M.-J. Yvonne Ou, J. Pei, L. E. Ratcliff, M. G. Reuter, A. C. Richie-Halford, N. A. Romero, H. Sekino, W. A. Shelton, B. E. Sundahl, W. Scott Thornton, E. F. Valeev, Á. Vázquez-Mayagoitia, N. Vence, T. Yanai, Y. Yokoi, *SIAM J Sci Comput* **2016**, 38, S123.
- [56] S. Lehtola, C. Steigemann, M. J. T. Oliveira, M. A. L. Marques, *SoftwareX* **2018**, 7, 1.
- [57] W. Ai, W. H. Fang, N. Q. Su, *J. Phys. Chem. Lett.* **2021**, 12, 1207.
- [58] Y. Akinaga, S. Ten-no, *Chem. Phys. Lett.* **2008**, 462, 348.
- [59] J. S. Kottmann, S. Alperin-Lea, T. Tamayo-Mendoza, A. Cervera-Lierta, C. Lavigne, T.-C. Yen, V. Verteletskyi, P. Schleich, A. Anand, M. Degroote, S. Chaney, M. Kesibi, N. G. Curnow, B. Solo, G. Tsilimigkounakis, C. Zendejas-Morales, A. F. Izmaylov, A. Aspuru-Guzik, *Quantum Sci Technol* **2021**, 6, 024009.
- [60] J. S. Kottmann, A. Anand, A. Aspuru-Guzik, *Chem. Sci.* **2021**, 12, 3497.
- [61] P. Jordan, E. Wigner, *Z. Phys.* **1928**, 47, 631.
- [62] J. R. McClean, N. C. Rubin, K. J. Sung, I. D. Kivlichan, X. Bonet-Monroig, Y. Cao, C. Dai, E. S. Fried, C. Gidney, B. Gimby, P. Gokhale, T. Häner, T. Hardikar, V. Havlicek, O. Higgott, C. Huang, J. Izaac, Z. Jiang, X. Liu, S. McArdle, M. Neeley, T. O'Brien, B. O'Gorman, I. Ozfidan, M. D. Radin, J. Romero, N. P. D. Sawaya, B. Senjean, K. Setia, S. Sim, D. S. Steiger, M. Steudtner, Q. Sun, W. Sun, D. Wang, F. Zhang, R. Babbush, *Quantum Sci Technol* **2020**, 5, 034014.
- [63] C. G. Broyden, *IMA J Appl Math* **1970**, 6, 76.
- [64] R. Fletcher, *Comput J* **1970**, 13, 317.
- [65] D. Goldfarb, *Math Comput* **1970**, 24, 23.
- [66] D. F. Shanno, *Math Comput* **1970**, 24, 647.
- [67] Y. Suzuki, Y. Kawase, Y. Masumura, Y. Hiraga, M. Nakadai, J. Chen, K. M. Nakanishi, K. Mitarai, R. Imai, S. Tamiya, T. Yamamoto, T. Yan, T. Kawakubo, Y. O. Nakagawa, Y. Ibe, Y. Zhang, H. Yamashita, H. Yoshimura, A. Hayashi, K. Fujii, *Quantum* **2021**, 5, 559.
- [68] Q. Sun, T. C. Berkelbach, N. S. Blunt, G. H. Booth, S. Guo, Z. Li, J. Liu, J. D. McClain, E. R. Sayfutyarova, S. Sharma, S. Wouters, G. K.-L. Chan, *WIREs Comput. Mol. Sci.* **2018**, 8, e1340.
- [69] Q. Sun, X. Zhang, S. Banerjee, P. Bao, M. Barbry, N. S. Blunt, N. A. Bogdanov, G. H. Booth, J. Chen, Z.-H. Cui, J. J. Eriksen, Y. Gao, S. Guo, J. Hermann, M. R. Hermes, K. Koh, P. Koval, S. Lehtola, Z. Li, J. Liu, N. Mardirossian, J. D. McClain, M. Motta, B. Mussard, H. Q. Pham, A. Pulkin, W. Purwanto, P. J. Robinson, E. Ronca, E. R. Sayfutyarova, M. Scheurer, H. F. Schurkus, J. E. T. Smith, C. Sun, S.-N. Sun, S. Upadhyay, L. K. Wagner, X. Wang, A. White, J. D. Whitfield, M. J. Williamson, S. Wouters, J. Yang, J. M. Yu, T. Zhu, T. C. Berkelbach, S. Sharma, A. Y. Sokolov, G. K.-L. Chan, *J Chem Phys* **2020**, 153, 024109.
- [70] D. G. A. Smith, L. A. Burns, A. C. Simmonett, R. M. Parrish, M. C. Schieber, R. Galvelis, P. Kraus, H. Kruse, R. Di Remigio, A. Alenaizan, A. M. James, S. Lehtola, J. P. Misiewicz, M. Scheurer, R. A. Shaw, J. B. Schriber, Y. Xie, Z. L. Glick, D. A. Sirianni, J. S. O'Brien, J. M. Waldrop, A. Kumar, E. G. Hohenstein, B. P. Pritchard, B. R. Brooks, H. F. Schaefer, Y. Alexander, K. P. Sokolov, A. Eugene DePrince, U. Bozkaya, R. A. King, F. A. Evangelista, J. M. Turney, T. Daniel Crawford, C. David Sherrill, *J Chem Phys* **2020**, 152, 184108.
- [71] B. P. Prascher, D. E. Woon, K. A. Peterson, T. H. Dunning, A. K. Wilson, *Theor. Chem. Acc.* **2011**, 128, 69.
- [72] H. Li, R. J. Le Roy, *J Chem Phys* **2006**, 125, 044307.
- [73] J. Toulouse, F. Colonna, A. Savin, *Phys. Rev. A* **2004**, 70, 062505.

- [74] P. Barletta, S. V. Shirin, N. F. Zobov, O. L. Polyansky, J. Tennyson, E. F. Valeev, A. G. Császár, *J Chem Phys* **2006**, *125*, 204307.
- [75] W. Kolos, L. Wolniewicz, *J Chem Phys* **1965**, *43*, 2429.
- [76] J. S. Kottmann, *Molecular Quantum Circuit Design: A Graph-Based Approach*. **2022**.
- [77] R. A. Kendall, J. Dunning, H. Thom, R. J. Harrison, *J Chem Phys* **1992**, *96*, 6796.
- [78] W. J. Hehre, R. Ditchfield, J. A. Pople, *J Chem Phys* **1972**, *56*, 2257.
- [79] T. H. Dunning, *J Chem Phys* **1989**, *90*, 1007.
- [80] M. Hapka, E. Pastorczak, A. Krzemińska, K. Pernal, *J Chem Phys* **2020**, *152*, 094102.
- [81] F. Edward, R. J. Harrison, C. C. Peterson, D. A. Penchoff, *Direct Determination of Optimal Real-Space Orbitals for Correlated Electronic Structure of Molecules*. **2022**.
- [82] M. C. Clement, J. Zhang, C. A. Lewis, C. Yang, E. F. Valeev, *J. Chem. Theory Comput.* **2018**, *14*, 4581.

SUPPORTING INFORMATION

Additional supporting information can be found online in the Supporting Information section at the end of this article.

How to cite this article: N. Poirier, J. S. Kottmann, A. Aspuru-Guzik, L. Mongeau, A. Najafi-Yazdi, *J. Comput. Chem.* **2024**, *45*(23), 1987. <https://doi.org/10.1002/jcc.27384>